ECS Transactions, 72 (37) 1-19 (2016)
10.1149/07237.0001ecst ©The Electrochemical Society

Optimizing "Artificial Leaf" Photoanode-Photocathode-Catalyst Interface Systems for Solar Water Splitting

S. H. Porter[a,b,#], S. Hwang[a,b,#], V. Amarasinghe[b,c], E. Taghaddos[d], V. Manichev[b,c], M. Li[b], G. Gardner[b], A. Safari[d], E. Garfunkel[a,b*], M. Greenblatt[a,b*], and G. C. Dismukes[a,b,*]

[a] Institute for Advanced Materials, Devices, and Nanotechnology, Rutgers University, New Brunswick, New Jersey 08854, USA
[b] Department of Chemistry, Rutgers University, New Brunswick, New Jersey 08854, USA
[c] Department of Physics, Rutgers University, New Brunswick, New Jersey 08854, USA
[d] Department of Materials Science & Engineering, Rutgers University, New Brunswick, New Jersey 08854, USA
[#] Authors contributed equally to this work, [*] To whom correspondence should be addressed

A novel dual photoabsorber interface: perovskite oxynitride ($SrNbO_2N$) deposited on silicon (100), and a H_2ER catalyst photoabsorber interface: (Ni_5P_4 or Ni_2P)-silicon, are fabricated. Titanium nitride (TiN) is introduced as a blocking layer between $Sr_2Nb_2O_7$ and Si (100), which produces clean interfaces. During the high temperature ammonolysis step needed to convert $Sr_2Nb_2O_7$ to $SrNbO_2N$, it is effective at blocking Nb and Si (but not Sr) migration. A half-cell cathode with the H_2ER catalyst (Ni_5P_4 or Ni_2P)-photoabsorber interface produces H_2 approaching best-in-class overpotentials for films (Ni_5P_4: 211mV vs RHE at 10mV/cm^2) with a 50mV/decade Tafel slope. Films are atomically smooth, except for surface phosphate that is removed during electrolysis.

Introduction

The intermittent nature of most renewable energy sources entails a need for large-scale energy storage. Energy can be stored safely, conveniently and with high density as chemical bonds. H_2 and O_2 derived from solar water splitting devices are the preferred renewable energy carriers allowing for conventional gas transport and long-term storage before a final conversion to electricity via fuel cells (1). Current photoelectrochemical (PEC) devices for water electrolysis suffer from one or more pitfalls, such as low stability, high cost, or low efficiency. Aims to address these needs have been investigated using a system that uses two sequential solar light absorbers (semiconductors) — in conjunction with catalysts for the oxygen evolution reaction (OER) and hydrogen evolution reaction (H_2ER). This tandem photoabsorber approach increases the theoretical solar to hydrogen efficiency from 12% to 22% (2). Further improvement is necessary because best-in-class systems using this approach reach only 10% efficiency (3) and operate with short lifetimes before failure (4). Of the four most common PEC configurations for water splitting (5), the fully integrated configuration denoted "artificial leaf" (6) is a popular target due to its ease of scaling and lower cost. This configuration eliminates ohmic

contacts in a wireless device but with lower system efficiencies observed. To enhance performance of such a device, while still maintaining simplicity, new materials are needed.

Tandem cell photoabsorbers employing single crystal (100) p-type Si (p-Si (100)) as the low band gap photocathode (E_g = 1.1 eV) require a wider gap material as photoanode that is approximately 1.8 eV for optimal efficiency (7). Selected perovskite oxynitrides, $ABO_{3-x}N_x$ (*A* = Sr and La; *B* = Ti, Nb, and Ta) powders have band gaps that lie near this value (8,9), have been suggested as good candidates for incorporation into photoelectrochemical systems (10,11), and initial results (as photoanodes) are promising. (12–14). Partial or full incorporation of nitrogen into an oxide host lattice reduces the bandgap considerably by adding less electronegative N 2p to the O 2p dominated valence band maximum, eg. 3.9 eV to 1.8 eV going from $SrNbO_{3.5}$ to $SrNbO_2N$ (15). A clean interface between the two photoabsorber materials can be achieved through cube-on-cube epitaxy (16) as both materials have (pseudo)cubic structures. Mismatched interfaces that lack delocalized electronic states commonly experience recombination of holes and electrons and therefore require an additional conductive layer as ohmic contact. A thin film of TiN was used to form the junction: $SrNbO_2N$:TiN:Si.

The silicon interface with electrolyte (cathode) is chemically unstable and must be passivated (17). We used a high performance non-precious metal catalyst, Ni_5P_4, which when fabricated as a pellet had H_2ER activities comparable to Pt (vs RHE) in acidic and alkaline solutions at 10mA/cm^2 (18). A thin film of this material was deposited onto silicon to create a photocathode. The full wireless device would have an OER catalyst/$SrNbO_2N$:TiN:Si/Ni_5P_4 (Figure 1). To better understand aspects affecting performance of this PEC configuration, two component interfaces of the full device were prepared: the photocathode, crystalline Ni-P thin films on a p-Si (100) substrate; and photoanode, $SrNbO_2N$/TiN/p-Si(100). Electrochemical performance, stability, interfacial diffusion, composition, and surface morphology of these materials and/or interfaces were studied.

Experimental

Chemicals and instrumentation

$Sr(NO_3)_2$ (Sigma Aldrich, 99.99%), $NbCl_5$ (Alfa, 99.9%), citric acid (Sigma Aldrich, 99%), 200 proof ethanol (Fisher Scientific, 100%), $NiSO_4$•$6H_2O$ (Sigma Aldrich, 99%), H_3PO_4 (Sigma Aldrich, >85%), NaH_2PO_2•H_2O (Sigma Aldrich, >99%), NaOH (Sigma Aldrich, 98%), and the TiN target (Kurt Lesker, 99.5%) were used as received.

X-ray diffraction (XRD) was carried out on a Bruker (Billerica, MA, USA) D8 Advance (Cu Kα1, 0.015° step size, 1-4 sec dwell time). GSAS was used for Rietveld refinements carried out on the $Sr_2Nb_2O_7$ PLD target. Isotropic thermal parameters of the atoms were constrained and refined together. Preferred orientation, expected for a sintered pellet (target), was accounted for by the spherical harmonics operator. Helium ion microscopy (HeIM) using a Carl Zeiss (Oberkochen, Germany) ORION PLUS SHIM was operated at 30kV for all imaging. Atomic force microscopy (AFM) images were generated using a Park Systems (Suwon, Korea) NX-10 with a Nanosensors (Neuchatel, Switzerland) PPP-NCHR tip in electrostatic force mode at room temperature in air. X-ray

photoelectron spectroscopy (XPS) measurements on a Thermo Scientific (Waltham, MA, USA) K-Alpha were carried out using charge compensation with spectra calibrated against adventitious carbon.

Preparation of the photoanode interface

$Sr_2Nb_2O_7$ powders were synthesized using the a sol-gel Pechini-inspired method (19) differing by replacing $SrCO_3$ with $Sr(NO_3)_2$ and by neglecting the use of ethylene glycol. Targets for pulsed laser deposition (PLD) were prepared by uniaxially pressing (105MPa) this powder, followed by sintering at 1400°C for 15 h with a 10°C/min ramp and cool. Sintered targets were phase pure by XRD (Figure 2), with proof of crystallinity and composition established by Rietveld refinement. Goodness-of-fit, bond, and atomic parameters are well matched with previously reported single crystal $Sr_2Nb_2O_7$ data(20). PLD was carried out using a KrF excimer laser Compex 205 (Lambda Physik, Coherent; Santa Clara, CA, USA) and a high vacuum chamber (Neocera; Beltsville, MD, USA). $Sr_2Nb_2O_7$ thin films were deposited on glassy carbon (HTW, Thierhaupten, Germany; Sigradur G) or p-Si (100) substrates. Processing parameters for the $Sr_2Nb_2O_7$ and TiN films were adapted from the literature (21; 22,23): laser intensity 2-8mJ/cm^2, substrate to target distance 7cm, O_2 partial pressure: 100 mtorr, pulses were 35 ns long, 150 – 300 mJ each, 10 Hz flash rate, and duration 10 – 30 min. For deposition of TiN, identical conditions to $Sr_2Nb_2O_7$ were used, except now under high vacuum, $<10^{-6}$ torr. These processing steps enabled the preparation of $SrNbO_2N$/TiN/glassy carbon thin film samples.

Preparation of the cathode

The substrate, a thin Ni film (5-12nm) on (100) oriented p-Si (IBM, Armonk, NY, USA; 9-18 Ωcm, 10^{16} B atoms/cm^3) was fabricated using standard methods to create H-terminated silicon (24). This was followed by deposition of nickel using an Angstrom Engineering (Kitchener, Canada) e-beam evaporator, at a rate of 1.0 Å/s and a base pressure of approximately 8.0 x 10^{-7} Torr. The low base pressure and slow evaporation rate ensured minimal incorporation of oxygen in the deposited metal films. Ni-P films were created on top of this substrate using potentiopulse techniques (25,26). Briefly, a bath at pH 3 (adjusted by NaOH) of 1.75 M NaH_2PO_2•H_2O, 0.5 M H_3PO_4, and a 0.1M total Ni concentration from $NiSO_4$•$6H_2O$ as well as $NiCl_2$•$6H_2O$, was used for electrochemical depositions. Working electrodes were prepared from the Ni/p-Si substrate by front-side contact where double-sided Cu tape secured a Cu wire as a lead and the area was sealed from electrolyte exposure using Teflon adhesive tape. All deposition solutions were Ar purged. Cyclic voltammetry was done at 1 V vs. RHE for film deposition using an Ametek (Berwyn, PA, USA) potentiostat with Ag/AgCl as reference and Pt foil as counter electrodes. These were separated from the main compartment by an anion exchange membrane preventing re-deposition of Pt on the working electrode during electrochemical deposition (27). The membrane is necessary because even miniscule amounts of redeposited Pt can falsely inflate catalytic H_2ER measurements (28). Crystallization of these amorphous films was achieved by a solvothermal method following a developed method for powders (18). Combination of these steps allows for the preparation of crystalline Ni-P/Ni_xSi_y/p-Si samples. Electrocatalytic H_2ER performance measurements were carried out as above, instead using a boron-doped diamond counter electrode.

Results & Discussion

$SrNbO_2N$: (p-Si <100> Interface

Epitaxy, the growth of a thin layer on the surface of a crystal so that the layer has the same structure as the underlying crystal, is desired because it facilitates efficient carrier transport across a heterojunction. For example, epitaxial $SrTiO_3$ on Si (100) has been demonstrated using molecular beam epitaxy (29,30), but few convincing examples exist using other techniques. Using the described fabrication techniques, $SrNbO_2N$ (a = 4.05Å) would be expected to suffer from interfacial defects, even though it has a similar lattice parameter as $SrTiO_3$ (a = 3.90Å). The incorporation of thin film TiN has been previously utilized as a conducting buffer layer between $SrTiO_3$ and Si(100) to achieve successful charge injection (21). For this reason, thin TiN was used at the interface between the wide and narrow gap photoabsorbers (Figure 1).

The epitaxy of the sample was evaluated before and after each step of the fabrication process: a) H-terminated Si substrate, b) post-TiN deposition, c) post-$Sr_2Nb_2O_7$, and d) post-ammonoylsis (Figure 3). Silicon contributes three peaks from 60 to 70 °2θ which do not interfere with the region of interest. (Orientation of the TiN layer is evidenced by its (200) Bragg peak at ~42 °2θ and grows-in via a Volmer-Weber-type 4-on-3 cube-on-cube mechanism (31). Similarly, after the next fabrication step, the (200) reflection from $Sr_2Nb_2O_7$ becomes visible, though weaker in intensity than the TiN reflection. Subsequent conversion of $Sr_2Nb_2O_7$ to $SrNbO_2N$ by ammonolysis, destroys the $Sr_2Nb_2O_7$ Bragg reflection. If (200) $SrNbO_2N$ epitaxy existed, a Bragg reflection at ~44 °2θ would be expected. Indeed, a broad peak appears as a weak shoulder next to TiN at that location, but the epitaxy and/or crystallization of the $SrNbO_2N$ phase is poor making verification of oxynitride formation using XRD futile.

PLD deposited $Sr_2Nb_2O_7$ and TiN thin films on Si (100) are 25 nm and 35 nm thick, respectively, with clean, defined interfaces (Figure 4, top). The discontinuities observed in the top film are residual from the substrate cleaving process when preparing the samples for HeIM cross-section imaging. The $Sr_2Nb_2O_7$ thin film was then subjected to ammonolysis conditions (eg., 900 °C, 0.5 – 15 h, 200 mL/min NH_3) and re-examined. This process did convert $Sr_2Nb_2O_7$ to $SrNbO_2N$ (lattice substituted N confirmed by XPS; not shown), but in doing so the interface was degraded (Figure 4, bottom). It is apparent that the TiN layer has increased porosity and that a thin 5-10 nm intergrowth is now present between the TiN and Si (100) layers.

Depth resolved XPS was performed to further investigate this post-ammonolysis intergrowth as well as the composition of the full stack (Figure 5). Adventitious carbon is present on the top surface of the composite, as is common with films that have been exposed to air. The $SrNbO_2N$ top film is strontium deficient, due to diffusion through TiN and aggregation at the silicon interface under the high temperature ammonolysis conditions. The thermodynamic driving force for formation of a $SrSiO_{3-x}$ localizes Sr at the Si interface. The TiN film is affected by the diffusion the process as well, with the composition shifting to more oxygen rich, and is better understood not strictly as TiN but as TiO_xN_y (32). However, the TiN layer is an effective diffusion barrier for niobium and silicon, with no apparent migration of these species post-anneal.

H_2ER Photocathode: Ni_5P_4:Ni:p-Si

An "artificial leaf" photocathode is typically comprised of a single crystal solar cell, highly n-type doped on p-Si (n^+p-Si) with the H_2ER catalyst integrated accordingly. This configuration allows for the injection of photogenerated electrons into the catalyst where externally unbiased water reduction can occur. However, prior to light measurements, electrochemical dark measurements on n-type silicon (n-Si), where no carrier injection should occur, were made in order to optimize catalytic HER overpotentials at current densities of 10 mA/cm^2.

Characterization. The XRDs of the prepared heterojunction devices have peaks associated with the substrate, p-Si <100>, at ~33 °2θ. A $NiSi_2$ interfacial layer is visible with peaks at ~46 and ~57 °2θ, that formed during the solvothermal crystallization process, where the Ni metal reacts with p-Si. A polycrystalline primary phase of Ni_2P forms following the solvothermal step (Figure 5; top, triangles), as well as an unknown secondary phase (squares). Conducting the reaction at higher temperatures increases phosphorus incorporation in the film, yielding crystalline Ni_5P_4 as the primary phase (bottom, stars), with Ni_2P as a secondary phase. Although the "Ni_5P_4" sample has a Ni_2P secondary phase, the relative mole percent for each phase present in these films is significant enough to allow general trends about a specific crystalline nickel phosphide phase's performance as a thin film.

Surface morphology and facet orientation has a strong influence on catalytic properties. The initial electrodeposition of the Ni-P thin films before solvothermal treatment produced an amorphous material by XRD (not shown), that is mechanically stable and pristine by visual inspection. To examine if the films change significantly during subsequent processing steps, the electrodeposited thin film was imaged by HeIM both before and after solvothermal treatment. The top surface of the film maintains its morphology after crystallization and no underlying substrate exposure is apparent
Figure 7).

The crystallized nickel phosphide films are uniform and conformal by AFM (Figure 8). Regardless of Ni-P phase present, Ni_2P (R_a = 2.4 nm) or Ni_5P_4 (1 nm), the synthesis method maintains a roughness similar to that of the substrate, which is atomically smooth (< 1 nm). The line profile (inset) reveals Z ranges from 0-12 nm with no systemic features. The continuity of the featureless surface during heterojunction processing (HeIM), which is maintained regardless of primary Ni-P phase (AFM), eliminates morphology as a possible factor when evaluating relative electrochemical activity between the two Ni-P films.

Because H_2ER catalysis is intimately dependent on interactions between the surface of the material and the electrolyte, it is important to identify what electronic states are present on the native material. The Ni 2p core level (Figure 9, top) has two dominant features, $2p_{3/2}$ at 853.8 eV and $2p_{2/1}$ at 871.2 eV. The satellite feature for each of these transitions is weak and broad, with the $2p_{3/2}$ satellite maximum near 862.6 eV and the $2p_{2/1}$ satellite unresolved above the baseline (near 877.5 eV). The $2p_{3/2}$ main peak is sharp with a weak shoulder. The sharp feature is characteristic of Ni metal (33), while the presence of the weak shoulder indicates a small amount of $Ni_3(PO_4)_2$ (34) or NiO_x (35).

The P 2p core level is also revealing (Figure 9, bottom). The $2p_{3/2}$ and $2p_{1/2}$ features at 129 eV and 133 eV, respectively, are best modelled as doublets. The former feature is indicative of binding associated with a transition metal phosphide (18) , while the latter is associated with a metal phosphate (34). The P 2p core level spectra corroborate well with the Ni 2p core level data in confirming the principle component in the prepared films is nickel phosphides, but also indicate the presence of a Ni-PO_4 species. Nickel phosphates are formed during air exposure and during positive electrolytic sweeps in water (18), but are not active as H_2ER catalysts, and therefore do not contribute to the activities reported here. They are removed below the H_2ER potential.

Electrochemistry. Before these heterojunctions are subjected to photo-driven processes, it is helpful to understand their electrochemical performance. In thin films of similar thickness and surface morphology, the Ni_5P_4 requires an overpotential that is 161 mV (measured at 10 mA/cm^2) lower than Ni_2P (**TABLE I**), in agreement with the trend seen for nanoparticles (18,36). The film resistances are comparable (20 vs. 18 Ω), as determined by electrochemical impedance spectroscopy (not shown). This eliminates electrical resistance as a significant factor in differentiating the observed activities. The Ni_5P_4 film has a Tafel slope that is 30 mV/dec less steep than Ni_2P. The reported Tafel slopes are intermediate between the known elementary H_2ER steps (Tafel = 30, Volmer = 120, and Heyrovsky = 40 mv/dec), as is common for multi-faceted or heterogeneous surfaces.

TABLE I. Electrochemical properties of heterojunction with thin film crystalline Ni_2P and Ni_5P_4 surfaces. All measurements in the dark in 0.5 M H_2SO_4.

	Ni_2P	**Ni_5P_4**
H_2ER overpotential at 10mA/cm^2 (mV) vs RHE	497	336
Film resistance (Ω)	18	20
Tafel Slope (mV/decade)	97	67

The H_2ER overpotentials of the prepared Ni_5P_4 (and Ni_2P) films follow the same trend as do the pelletized nanoparticles of the same materials (18), where the H_2ER of Ni_5P_4 nanoparticles is comparable to Pt foil on a geometric area basis, but, the overall performance of the thin film is inferior to the pelletized nanoparticles. To further investigate the nature of this discrepancy, three Ni_5P_4 films with increasing thickness were created. This was achieved by sequentially increasing the number of potentio-pulse steps during electrodeposition of the films. For thin to thick film deposition, respectively, the total charge passed was 1.2 C, 1.9 C, and 28.6 C. There is a clear trend that emerges: with increasing thickness, the H_2ER overpotential decreases (Figure 11). This observation is consistent other Ni-P (37) or Pd (38) HER catalysts, and is possibly explained by surface reorganization, or diminished substrate to film interactions (ligand effect), or lateral strain-induced pseudomorphism (39). The thickest Ni_5P_4 sample prepared had the lowest observed overpotential, which was more active catalytically than MoP, within 10mV of CoP (40). This result is notable because the latter compound is one of the most active crystalline, non-precious metal H_2ER catalysts reported to date on a geometrical surface area basis (40). Furthermore, material costs (spot prices) for nickel are approximately half that of cobalt.

Conclusion

A tandem photoabsorber comprised of a perovskite oxynitride on p-Si separated by a TiN recombination layer was prepared using PLD. Epitaxial growth of thin film TiN on crystalline Si was observed, but not between the TiN and $SrNbO_2N$ layers. The latter was attributed to the harsh post-processing steps (ammonolysis) needed to convert the as-deposited $Sr_2Nb_2O_7$ film to $SrNbO_2N$. Although the TiN layer is effective at blocking Si and Nb migration during ammonolysis, thermal diffusion of Sr from $Sr_{1-x}NbO_2N$ to the Si/TiN interface occurs. A p-Si/Ni_5P_4 cathode interface was prepared by cathodic pulse deposition followed by solvothermal annealing to form smooth, crystalline thin films. Auto-oxidation of the Ni-P films occurred leading to minor Ni-oxide/Ni-phosphate formation that could be removed electrolytically and was inconsequential for H_2ER activity. Thicker Ni_5P_4 films operate more efficiently than thin ones (significantly less overpotential), suggesting possible surface reconstruction. These films performed H_2ER as well as other best-in-class transition metal phosphides (CoP). Insights gained from studying these interfaces have significantly advanced progress towards development of a wireless, tandem PEC utilizing oxynitride perovskites as photoabsorbers and non-precious metal water splitting catalysts.

Acknowledgments

Funding for this research was provided by DOE/NSF grant: CBET-1433492. G.C.D., M.G., and E.G. are grateful to the Institute for Advanced Materials, Devices, and Nanotechnology for providing facilities and auxiliary support.

References

1. A. J. Bard and M. A. Fox, *Acc. Chem. Res.*, **28**, 141–145 (1995).
2. M. S. Prévot and K. Sivula, *J. Phys. Chem. C*, **117**, 17879–17893 (2013) http://dx.doi.org/10.1021/jp405291g.
3. H. Döscher, J. L. Young, J. F. Geisz, J. A. Turner, and T. G. Deutsch, *Energy Environ. Sci.*, **9**, 74–80 (2016).
4. R. J. Britto et al., *J. Phys. Chem. Lett.*, **7**, 2044–2049 (2016) http://dx.doi.org/10.1021/acs.jpclett.6b00563.
5. J. W. Ager, M. R. Shaner, K. A. Walczak, I. D. Sharp, and S. Ardo, *Energy Environ. Sci.*, **8**, 2811–2824 (2015) http://dx.doi.org/10.1039/C5EE00457H.
6. S. Y. Reece et al., *Science (80-.).*, **334**, 645–648 (2011).
7. S. Hu, C. Xiang, S. Haussener, A. D. Berger, and N. S. Lewis, *Energy Environ. Sci.*, **6**, 2984–2993 (2013).
8. S. H. Porter et al., *Chem. Mater.*, **2**, 150226095140008 (2015) http://pubs.acs.org/doi/abs/10.1021/cm5044599.
9. S. H. Porter, Z. Huang, and P. M. Woodward, *Cryst. Growth Des.*, **14**, 117–125 (2014) http://dx.doi.org/10.1021/cg401230a.
10. I. E. Castelli et al., *Energy Environ. Sci.*, **5**, 5814–5819 (2012).
11. Y.-I. Kim, P. M. Woodward, K. Z. Baba-Kishi, and C. W. Tai, *Chem. Mater.*, **16**, 1267–1276 (2004).

12. M. Higashi, K. Domen, and R. Abe, *J. Am. Chem. Soc.*, **135**, 10238–10241 (2013).
13. K. Maeda, M. Higashi, B. Siritanaratkul, R. Abe, and K. Domen, *J. Am. Chem. Soc.*, **133**, 12334–12337 (2011).
14. A. Kasahara et al., *J. Phys. Chem. A*, **106**, 6750–6753 (2002).
15. S. G. Ebbinghaus, R. Aguiar, A. Weidenkaff, S. Gsell, and A. Reller, *Solid State Sci.*, **10**, 709–716 (2008) http://linkinghub.elsevier.com/retrieve/pii/S1293255807000581.
16. S. H. Baek and C. B. Eom, *Acta Mater.*, **61**, 2734–2750 (2013) http://dx.doi.org/10.1016/j.actamat.2012.09.073.
17. A. Valance, *Phys. Rev. B*, **52**, 8323 (1995).
18. a. B. Laursen et al., *Energy Environ. Sci.*, **8**, 1027–1034 (2015) http://pubs.rsc.org/en/content/articlehtml/2015/ee/c4ee02940b\nhttp://xlink.rsc.org/?DOI=C4EE02940B.
19. M. Yoshino, M. Kakihana, W. S. Cho, H. Kato, and A. Kudo,.
20. P. Daniels et al., *Acta Crystallogr. Sect. B Struct. Sci.*, **58**, 970–976 (2002).
21. W. Wu, K. H. Wong, and C. L. Choy, *Thin Solid Films*, **360**, 103–106 (2000).
22. J. Narayan et al., *Appl. Phys. Lett.*, **61**, 1290–1292 (1992).
23. K. R. Balasubramaniam et al., *J. Solid State Chem.*, **181**, 705–714 (2008).
24. D. B. Fenner, D. K. Biegelsen, and R. D. Bringans, *J. Appl. Phys.*, **66** (1989).
25. M.-S. Wu and J.-F. Wu, *Chem. Commun.*, **49**, 10971–10973 (2013) http://dx.doi.org/10.1039/C3CC45670F.
26. S. A. Lajevardi and T. Shahrabi, *Appl. Surf. Sci.*, **256**, 6775–6781 (2010).
27. S. Cherevko, A. R. Zeradjanin, G. P. Keeley, and K. J. J. Mayrhofer, *J. Electrochem. Soc.*, **161**, H822–H830 (2014).
28. A. A. Topalov et al., *Angew. Chemie Int. Ed.*, **51**, 12613–12615 (2012) http://dx.doi.org/10.1002/anie.201207256.
29. R. A. McKee, F. J. Walker, and M. F. Chisholm, *Phys. Rev. Lett.*, **81**, 3014–3017 (1998).
30. R. A. McKee, F. J. Walker, J. R. Conner, E. D. Specht, and D. E. Zelmon, *Appl. Phys. Lett.*, **59**, 782–784 (1991).
31. P. . Willmott, R. Timm, and J. . Huber, *Appl. Surf. Sci.*, **127**, 105–110 (1998).
32. M. Dryga, C. Czosnek, R. T. Paine, and J. F. Janik,.
33. A. P. Grosvenor, M. C. Biesinger, R. S. C. Smart, and N. S. McIntyre, *Surf. Sci.*, **600**, 1771–1779 (2006).
34. J.-J. Li et al., *RSC Adv.*, **5**, 41721–41728 (2015) http://xlink.rsc.org/?DOI=C5RA06050H.
35. J. You et al., *Nat Nano*, **11**, 75–81 (2016) http://dx.doi.org/10.1038/nnano.2015.230.
36. E. J. Popczun et al., *J. Am. Chem. Soc.*, **135**, 9267–9270 (2013) http://dx.doi.org/10.1021/ja403440e.
37. I. Paseka, *Electrochim. Acta*, **47**, 921–931 (2001) http://www.sciencedirect.com/science/article/pii/S0013468601008143.
38. L. A. Kibler, *Electrochim. Acta*, **53**, 6824–6828 (2008).
39. L. A. Kibler, *ChemPhysChem*, **7**, 985–991 (2006).
40. T. R. Hellstern, J. D. Benck, J. Kibsgaard, C. Hahn, and T. F. Jaramillo, *Adv. Energy Mater.*, **6**, n/a–n/a (2016) http://doi.wiley.com/10.1002/aenm.201501758.

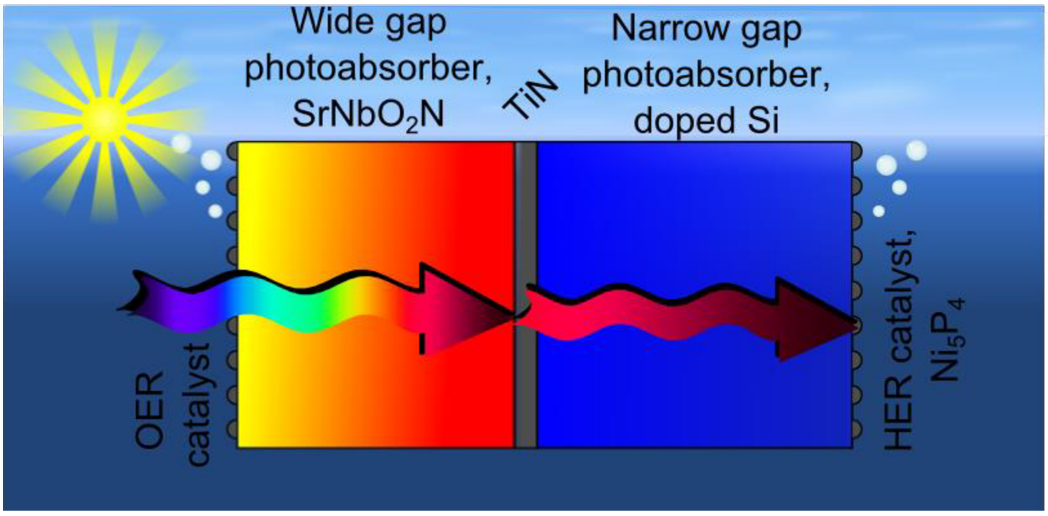

Figure 1. The configuration of a wireless, tandem PEC device on a silicon substrate utilizing a perovskite oxynitride ($SrNbO_2N$) and a H_2ER catalyst (Ni_5P_4).

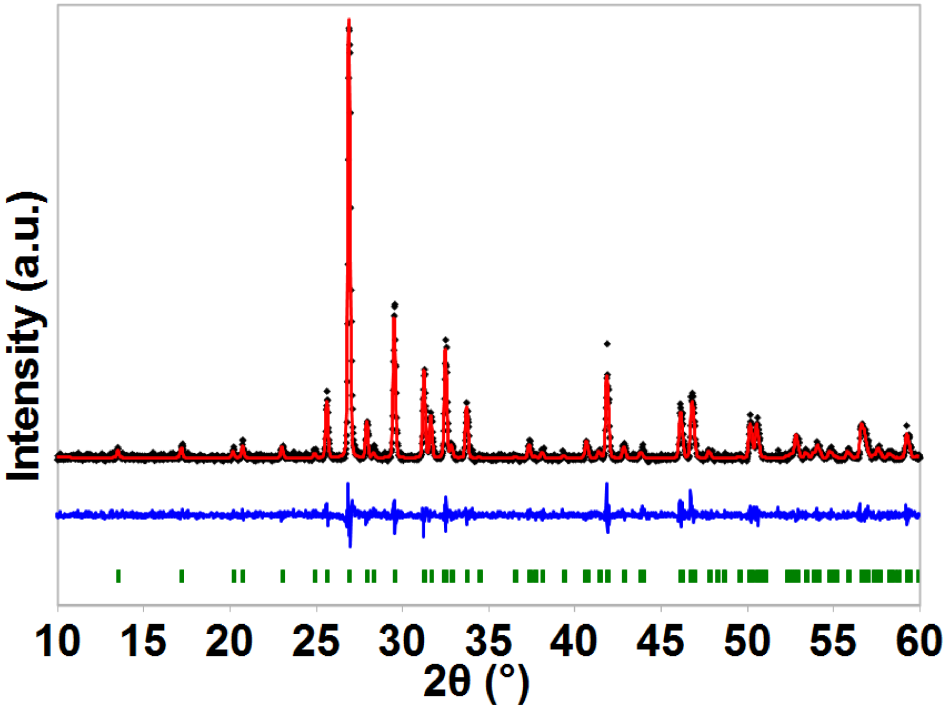

Figure 2. Laboratory XRD Rietveld refinement of the $Sr_2Nb_2O_7$ PLD target. Observed (black), difference (blue), calculated (red), and Bragg reflections (green) are compared.

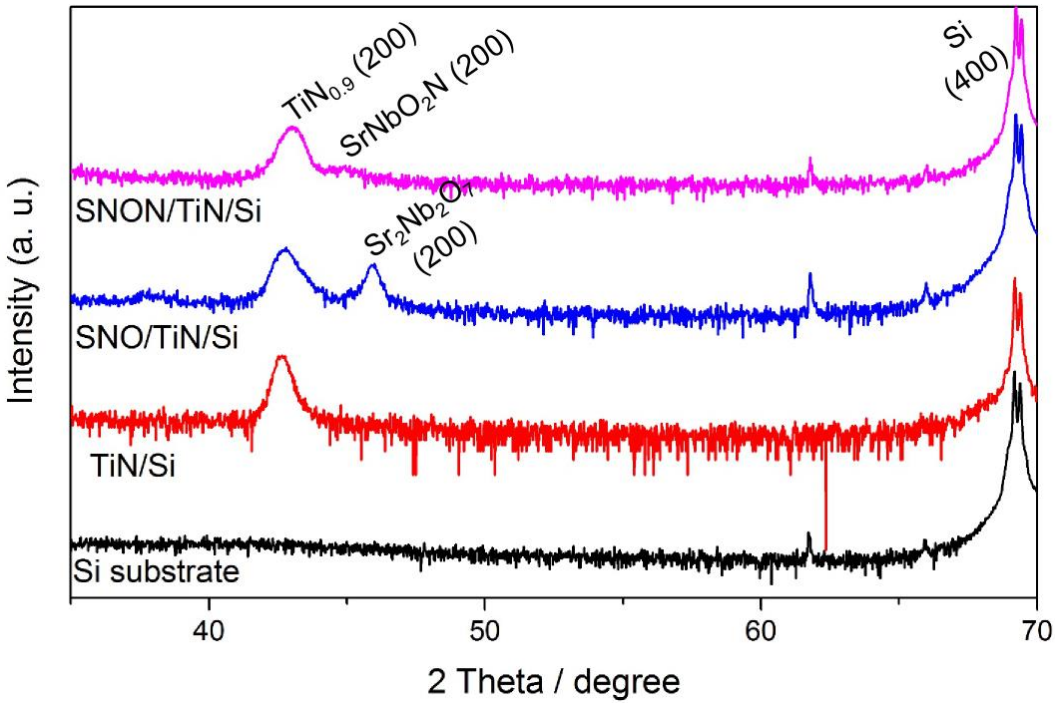

Figure 3. Examination of cube-on-cube epitaxy in the $SrNbO_2N$/TiN/Si<100> system

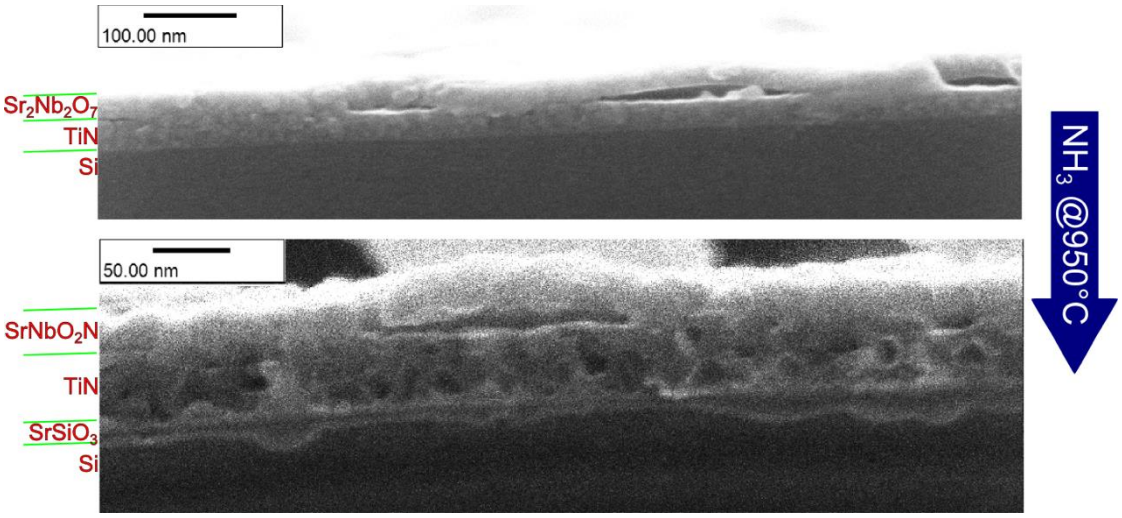

Figure 4. Morphology of a Sr-Nb-O(-N) thin film pre- and post-ammonolysis

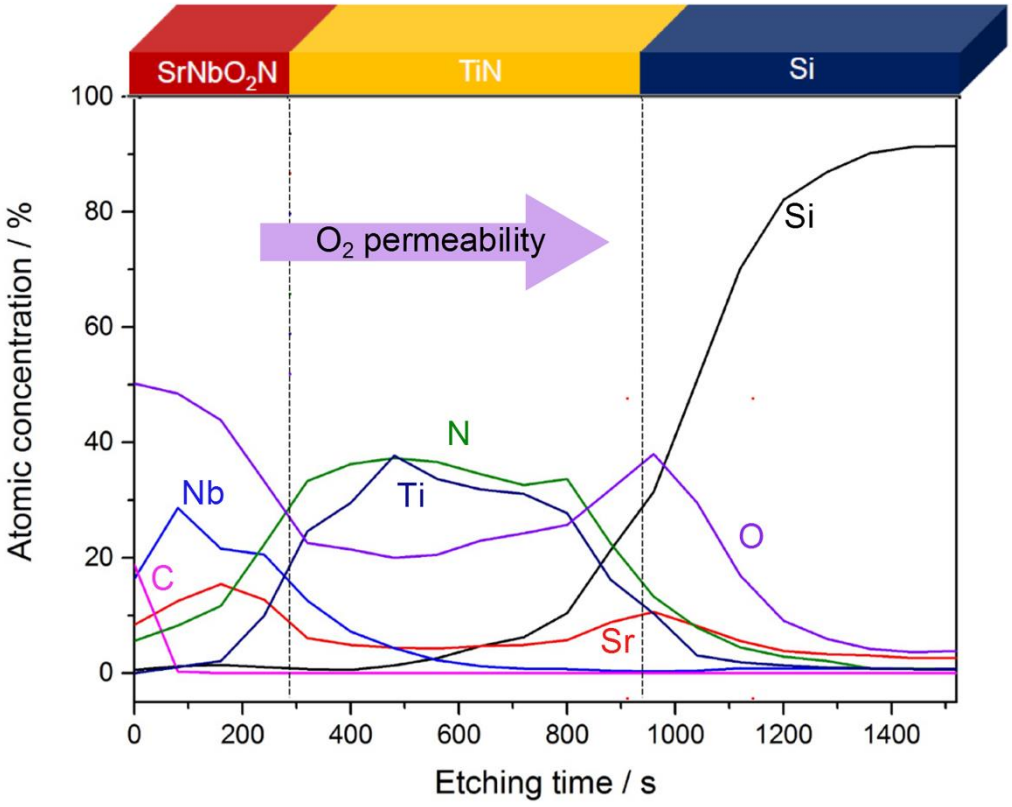

Figure 5. Ion (Ar^+) sputtered depth profile of $SrNbO_2N$/TiN/p-Si thin film.

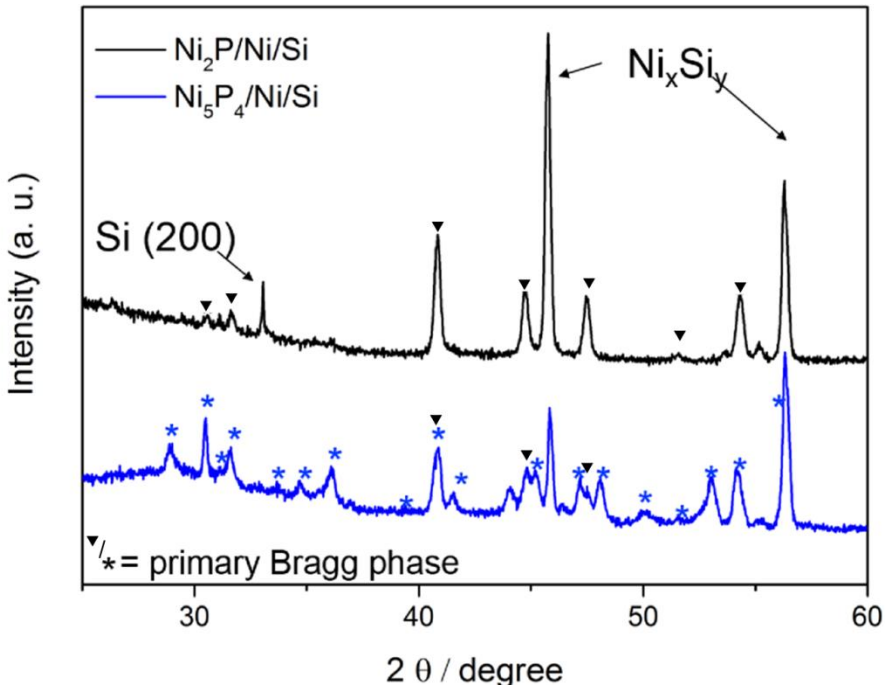

Figure 6. XRDs of Ni-P thin films on Ni (5nm)/p-Si (100) substrates.

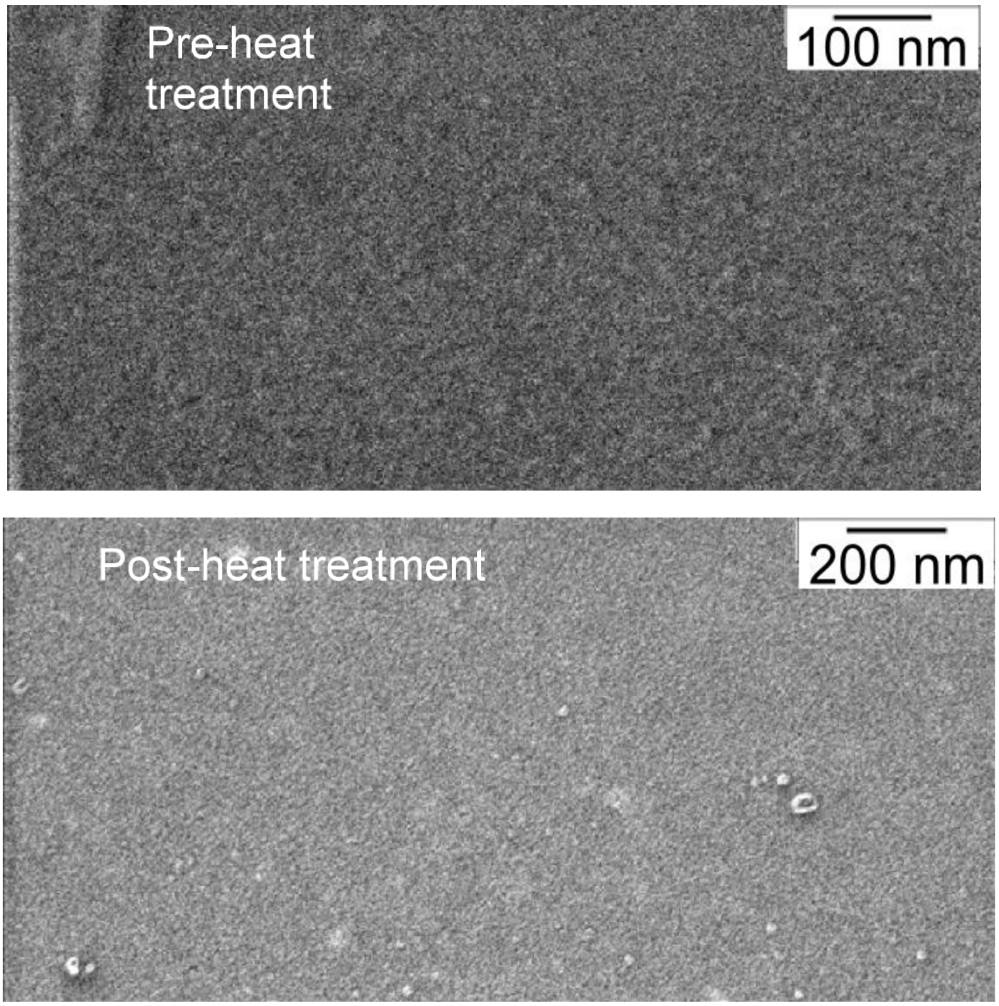

Figure 7. HeIM images of pre- and post-solvothermal treatment of Ni_5P_4 films.

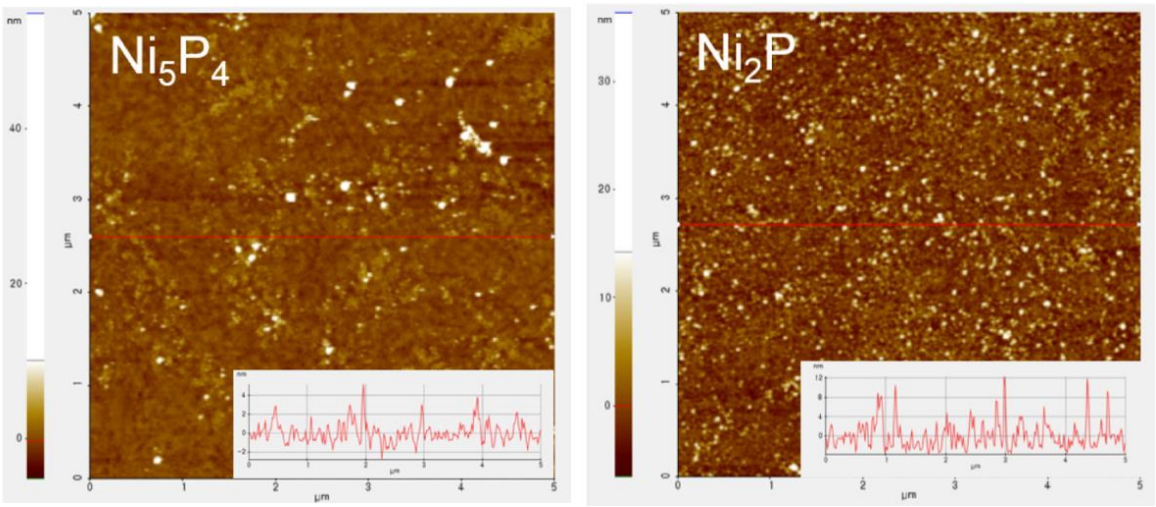

Figure 8. AFM of Ni-P compounds.

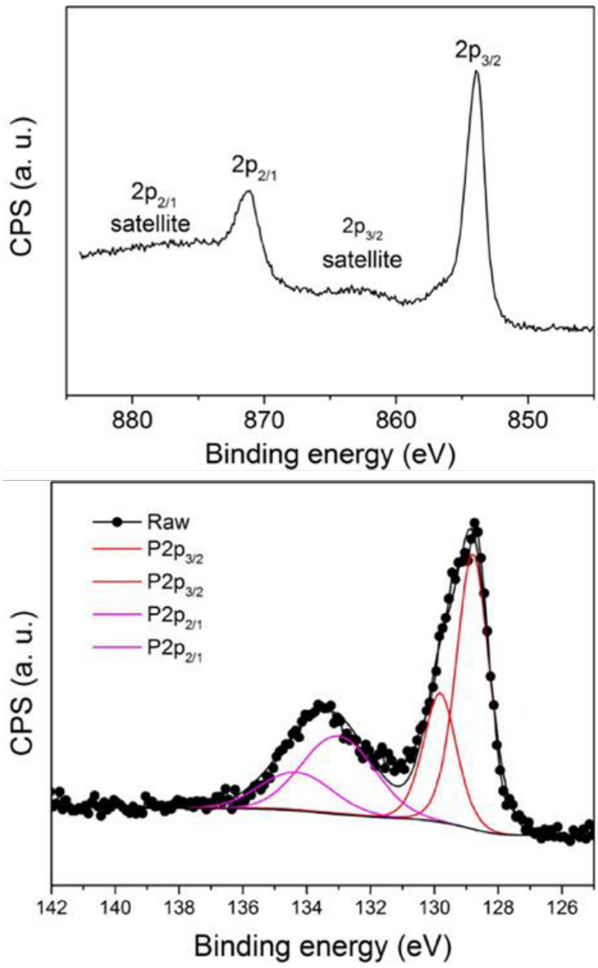

Figure 9. Core level XPS of Ni_5P_4.

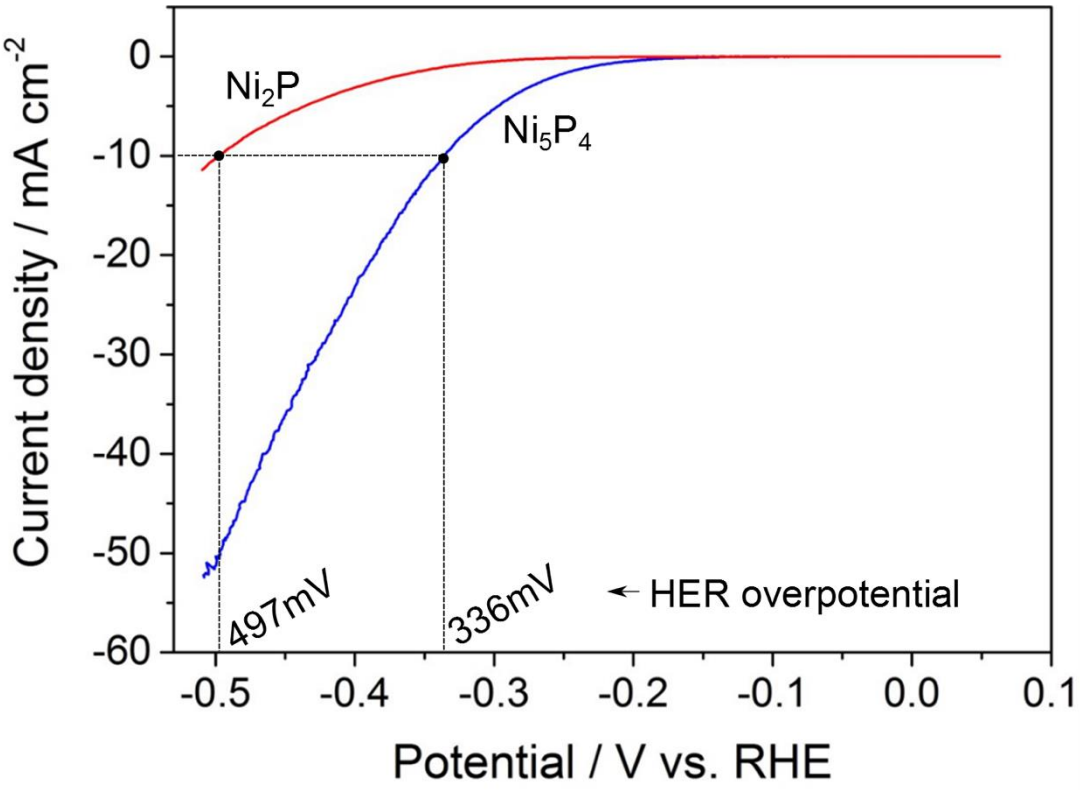

Figure 10. H_2ER activity of Ni-P films on Ni/p-Si in acid (0.5M H_2SO_4)

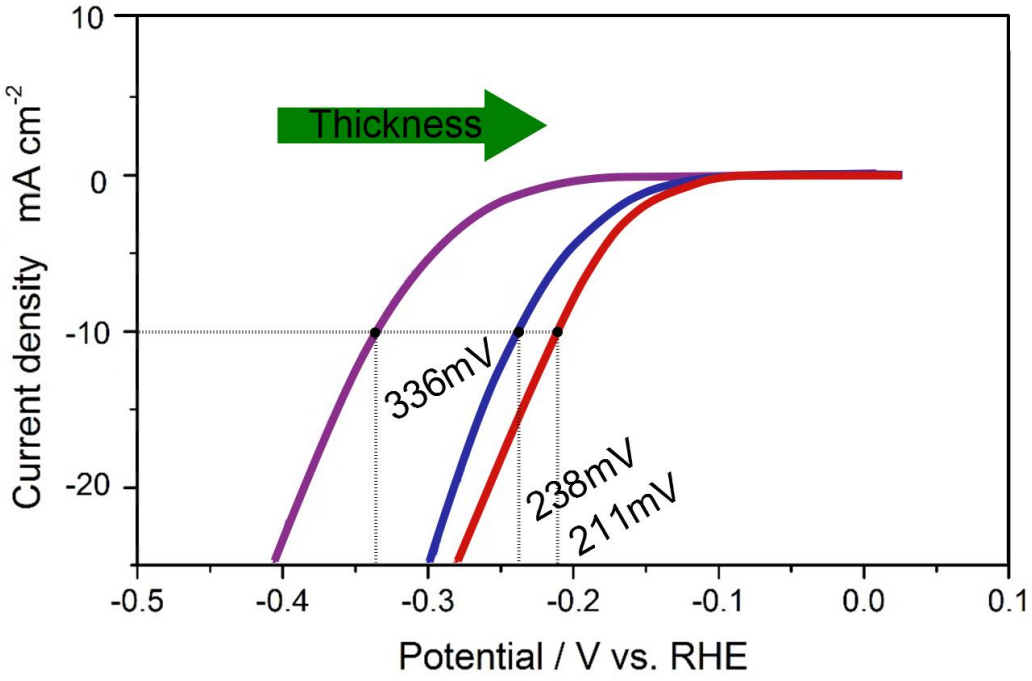

Figure 11. Thickness dependence of H_2ER electrocatalytic performance at 10mA/cm^2 for Ni_5P_4 films on Ni/p-Si in acid (0.5M H_2SO_4).